Bayesian Exploration of Multivariate Orographic Precipitation Sensitivity for Moist Stable and Neutral Flows

Samantha A. Tushaus*

Space Science and Engineering Center, Madison, WI, USA

Derek J. Posselt

University of Michigan, Ann Arbor, MI, USA

M. Marcello Miglietta

Institute of Atmospheric Sciences and Climate (ISAC), Italian National Research Council (CNR), Lecce, Italy

Richard Rotunno, Luca Delle Monache

National Center for Atmospheric Research, Boulder, CO, USA

* *Corresponding author address*: Samantha A. Tushaus, Space Science and Engineering Center, University of Wisconsin-Madison, 1225 W. Dayton Street, Madison, WI 53706-1612. Email: sam.tushaus@ssec.wisc.edu

Abstract

Recent idealized studies have examined the sensitivity of topographically forced rain and snowfall to changes in mountain geometry and upwind sounding in moist stable and neutral environments. These studies were restricted by necessity to small ensembles of carefully chosen simulations. This research extends the earlier studies by utilizing a Bayesian Markov chain Monte Carlo (MCMC) algorithm to create a large ensemble of simulations, all of which produce precipitation concentrated on the upwind slope of an idealized Gaussian bell-shaped mountain. MCMC-based probabilistic analysis yields information about the combinations of sounding and mountain geometry favorable for upslope rain, as well as the sensitivity of orographic precipitation to changes in mountain geometry and upwind sounding. Many different combinations of flow, topography, and environment produce very similar rainfall. Exploration of the multivariate sensitivity of rainfall to changes in parameters reveals tipping points in the system, around which a small change in environmental characteristics produces a very large change in rainfall amount and distribution. Detailed examination of model output reveals high sensitivity in the mountain wave breaking behavior to be the primary cause of these rapid changes in rainfall.

1. Introduction

More than half a century of orographic precipitation research has discovered that topographically forced rainfall is sensitive to mountain shape, three-dimensional winds, surface properties, the characteristics of the upstream sounding, and details of cloud microphysical processes (Sawyer 1956; Smith 1979; Barcilon et al. 1979; Durran and Klemp 1982, 1983; Miglietta and Buzzi 2001; Colle 2004). In many regions, large-scale moist stable and neutral flow is instrumental in generating upslope precipitation in mountainous terrain (Douglas and Glasspoole 1947; Sawyer 1956; Sarker 1967; Doswell et al. 1998; Buzzi and Foschini 2000; Rotunno and Ferretti 2003; Miglietta and Rotunno 2005, 2006). This type of flow has been recently analyzed as *atmospheric rivers* interacting with orography along the U.S. West Coast (Ralph et al. 2004; Ralph et al. 2005; Niemann et al. 2011; Ralph and Dettinger 2011; Rutz et al. 2014).

A number of field campaigns have been conducted with the goal of improved understanding of stable and moist neutral orographic precipitation. Precipitation along the United States Intermountain West and mountainous West Coast was the focus of the PACific Land-falling JETs campaign (PACJET; Niemann et al. 2002), the Improvement of Microphysical PaRameterization through Observational Verification Experiment (IMPROVE and IMPROVE-II; Stoelinga et al. 2003), the Intermountain Precipitation EXperiment (IPEX; Schultz et al. 2002), and the Sierra Hydrometeorology Atmospheric Rivers Experiment (SHARE; Kingsmill et al. 2006). The Mesoscale Alpine Programme (MAP; Bougeault et al. 2001; Rotunno and Houze 2007) studied storm systems and moist flow impinging on the European Alps. All of these studies confirmed that mesoscale orographic effects on airflow determine the location, intensity, and amount of observed rainfall. Rotunno and Ferretti (2003) reported on two intensive observing periods in MAP that observed nearly moist-neutral stability during the passage of synoptic storm systems. In addition, Rotunno and Houze (2007), in a MAP summary paper, recommended a thorough exploration of the orographic precipitation parameter space to better understand its sensitivity to changes in upstream conditions. Their findings and the broader outcomes of MAP motivated a number of numerical modeling studies, including the idealized studies of Miglietta and Rotunno (2005, 2006, 2009, 2010; hereafter MR05, MR06, MR09, and MR10, respectively).

These studies showed that the complex interrelationship between controlling atmospheric and topographic factors and resulting orographic precipitation makes it difficult to clearly discern (1) which combinations of factors produce a given distribution of precipitation, and (2) how multiple simultaneous changes in the thermodynamic sounding, flow, and mountain geometry enhance or suppress precipitation. MR05 and MR06 examined the sensitivity of steady-state orographic precipitation in moist neutral flow to changes in temperature profile, mountain height and width, and cloud microphysics complexity. They classified their rainfall distributions into categories according to mountain height. However, classification became difficult as mountain width and profile temperature were allowed to vary, implying complexity in the relationships between mountain geometry, the upwind sounding, and resulting surface precipitation.

While MR05 and MR06 focused on moist neutral flow, a scenario adequately characterized by a two-dimensional framework, conditionally unstable flows are more complex (MR09; MR10; Miglietta and Rotunno 2012, 2014). They are associated with a succession of three-dimensional, time-dependent cloud cells, which together may be considered a class of turbulent flow. MR09 and MR10 examined the role of buoyancy in determining surface precipitation by conducting 80 numerical experiments with varying values of convective available potential energy (CAPE) and downdraft CAPE (DCAPE), wind speed, and mountain height and width. They discovered a complicated relationship between the chosen control parameters and precipitation, one that changed depending on the region of parameter space examined. Studies of both stable and unstable flows indicate that controls on orographic precipitation are multivariate, and an exploration of the connections between different factors of influence will require a more complete exploration of parameter (co)variability than has previously been attempted.

In this paper we extend the analysis of MR05 and MR06 to address two fundamental science questions concerning precipitation generated by moist neutral flow over a barrier:

1. What is the quantitative sensitivity of topographically forced precipitation to changes in mountain geometry, wind profiles, and the thermodynamic environment?
2. Which combinations of physical states and mountain configurations produce a given distribution and intensity of upslope precipitation?

Both questions can be answered by systematically varying the factors that control upslope precipitation in a cloud resolving model and examining the results. The challenge is the computational expense of examining every parameter permutation necessary to thoroughly explore multivariate sensitivity in the orographic precipitation system. We surmount this challenge using a Bayesian methodology, supplemented by a stochastic sampling procedure (section 2), to answer our research questions in a systematic and objective manner. We outline our results in detail in section 3, provide further discussion and analysis in section 4, and summarize our major conclusions in section 5.

2. Numerical Methods

2.1 CM1 Model

The Cloud Model 1 (CM1) described in Bryan and Fritsch (2002) (http://www2.mmm.ucar.edu/people/bryan/cm1) was designed for study of cloud-scale atmospheric processes. It uses the vertically implicit, time-splitting Klemp-Wilhelmson technique to calculate the non-hydrostatic compressible equations of mass, momentum, energy, and moisture. A fifth-order advection scheme operates in the horizontal and vertical for both scalars and velocities. CM1 uses a terrain-following vertical coordinate, and subgrid-scale turbulence is parameterized using a turbulent kinetic energy closure (Deardorff 1980).

While ice microphysical processes are known to exert a significant effect on orographic precipitation (Stoelinga et al. 2003), parameterizations are highly sensitive to assumed ice density, particle shape, and fall speed (Posselt and Vukicevic 2010). This research represents the first time a complete multivariate orographic precipitation sensitivity analysis has been conducted. As such, we consider only liquid processes in our experiments and utilize a warm-rain (Kessler 1969) scheme. Tests of various CM1 model simulations in moist stable and neutral conditions revealed that the model reaches a steady precipitation distribution after approximately 10 simulated hours (MR05, MR09). While three dimensions and 1 km grid spacing, or finer, is typically required to model deep convection (Bryan et al. 2003), moist neutral flow can be realistically simulated using a two-dimensional domain and 2 km grid spacing (MR05, MR06). The simulations in this study are performed with the CM1, release 17, and have a 2D domain 800 km in length. The minimum number of grid points (three) was used in the y-direction, as CM1 does not run in parallel in purely 2D mode. Horizontal grid spacing is 2 km and stretches to 6 km over 50 grid points at each end of the x-domain. The domain is 20 km in height with 59 vertical levels. The vertical grid spacing is 250 m from the surface to z = 9,000 m, increases to 500 m from z = 9,000 m to z = 10,500 m, and stays constant at 500 m above z = 10,500 m (as in

MR05). Lateral boundary conditions are all open-radiative, the lower boundary is free-slip, and a Rayleigh damping layer is applied to the top 6 km of the domain to prevent reflection of vertically propagating gravity waves. The chosen domain size and grid spacing produced realistic upslope precipitation while requiring only 90 seconds of wall clock run time. Comparisons between the configuration described above and a reference simulation run with 250 m horizontal and vertical grid spacing produced nearly identical results (not shown).

In this study, the flow characteristics, cloud properties, and resulting precipitation amount and distribution are governed by only six parameters: mean wind speed ($\bar{u}$), squared moist Brunt-Väisälä frequency (N_m^2), surface potential temperature (θ_{sfc}), profile relative humidity (RH), mountain height (H_{mtn}), and mountain half-width (W_{mtn}). Mean wind speed and direction, relative humidity, and N_m^2 are constant with height at the upwind boundary. Precipitation is binned into six regions on the mountain: three each on the upwind and downwind slopes (Fig. 1). Initial conditions consist of an idealized moist neutral sounding (MR05), continuously advected into the domain from the west (upwind) boundary (Fig. 2). The idealized bell-shaped mountain is constructed from the same function used in MR05, MR06, MR09, and MR10, where mountain height is defined as

$$h(x) = \frac{h_m}{1 + [(x - x_0)/a]^2}. \quad (1)$$

Here x is the position within the domain in meters, the mountain is centered on x_0, h_m is maximum mountain height, and a is the mountain half-width in meters. The mountain height and half-width parameters control the mountain geometry.

2.2 Sensitivity Analysis, Bayes Theorem, and MCMC Algorithms

The fundamental goals of this study are to (1) explore which combinations of mountain geometry and upwind sounding parameters result in similar orographic precipitation amount and spatial resolution, and (2) assess the sensitivity of precipitation to changes in sounding and mountain geometry. If precipitation expresses particular sensitivity to changes in wind speed, for example, in theory a narrow range of wind speed values will define a given precipitation distribution. A challenge comes in the form of *mitigating factors*; for example, an increase in wind speed may be compensated by a decrease in relative humidity in order to produce equivalent water vapor-to-precipitation conversion rates. If only a few factors control precipitation rate, it is straightforward to assess the parameter-precipitation relationship and the sensitivity of precipitation to parameter changes using successive numerical model runs. However, for more than 3-4 controlling parameters, the computational challenge of simulating precipitation for every possible combination of parameters (*brute force sensitivity analysis*) becomes impractical. In fact, the computational expense grows as M^N, where M is the number of discrete values of input parameters and N is the number of parameters.

We may reduce the computational burden by realizing that some model runs from the brute force sensitivity analysis do not produce a precipitation distribution similar to the distribution of interest. As in an optimization problem, we seek sets of input parameters that fit a given precipitation distribution while avoiding sets of input parameters with a poor fit. However, unlike an optimization problem, the search for sets of input parameters must allow for the possibility of multiple solutions, or multiple parameter sets that produce an equally good fit to the given precipitation distribution. *Markov chain Monte Carlo* (MCMC) *algorithms* comprise a class of Bayesian methods that explore a parameter space and assess model output sensitivity, while avoiding parameter sets that produce a poor fit to the chosen observations.

Let a set of upwind sounding and mountain geometry parameters be represented in a six-element vector **x** = [$\bar{u}$, N_m^2, θ_{sfc}, RH, H_{mtn}, W_{mtn}], and let the given precipitation distribution (binned into six mountain regions) be represented in a six-element vector **y** = [P1,P2,P3,P4,P5,P6]. All input parameters in **x** are assigned realistic ranges, outlined in Table 1, with equal (Uniform) probability of occurrence. A CM1 simulation run with a specified set of control parameters (Table 1) produces the given precipitation distribution **y** (values in Table 2). Our fundamental goals may now be expressed as (1) exploring which values of **x** produce a given precipitation distribution **y**, and (2) assessing the sensitivity of **y** to changes in the input parameters **x**. Exploring the probability of **x** given **y**, or $P(\mathbf{x}|\mathbf{y})$, allows us to (1) quantify the probability that a certain set of parameters **x** produces the given precipitation distribution **y**, and (2) use the probability density function $P(\mathbf{x}|\mathbf{y})$ to describe the sensitivity of precipitation **y** to input parameters **x**. Bayes' Theorem defines $P(\mathbf{x}|\mathbf{y})$:

$$P(\mathbf{x}\,|\,\mathbf{y}) = \frac{P(\mathbf{y}\,|\,\mathbf{x})P(\mathbf{x})}{P(\mathbf{y})} \; . \tag{2}$$

$P(\mathbf{x})$ is the Bayesian *prior*, which represents our knowledge of the elements of **x** before **y** is known. In our study $P(\mathbf{x})$ corresponds to a bounded Uniform probability of occurrence for each possible value of the parameters in **x**; no combination of parameters is more likely than any others within the provided range. $P(\mathbf{y}|\mathbf{x})$, termed the *likelihood,* represents the probability that the parameters **x** are the control parameters, given the precipitation rates **y** calculated in the control simulation, and takes into account measurement uncertainty. We have defined the precipitation rate standard deviation as 2 mm hr^{-1}, and assumed a Gaussian distribution for the likelihood. Note that one may assume other probability distributions for the likelihood, such as the Log-Normal distribution used in Posselt et al. (2008). $P(\mathbf{y})$ is a normalizing factor that integrates over all possible precipitation rates $\mathbf{y}$ produced by all possible parameters $\mathbf{x}$, and ensures that the left-hand side of Eq. (2) integrates to 1. $P(\mathbf{x}|\mathbf{y})$ is termed the Bayesian *posterior*, and describes the probability that a set of input parameters $\mathbf{x}$ produced a given precipitation distribution $\mathbf{y}$. For example, a single maximum in the posterior distribution indicates a unique relationship between input parameters $\mathbf{x}$ and orographic precipitation distribution $\mathbf{y}$; small dispersion in $P(\mathbf{x}|\mathbf{y})$ indicates high sensitivity of $\mathbf{y}$ to changes in $\mathbf{x}$.

As mentioned earlier, a brute force calculation of the above probabilities for all combinations of the six input parameters $\mathbf{x}$ is computationally intractable. The MCMC algorithm reduces the computational burden by constructing a *guided random walk* that samples the posterior probability distribution $P(\mathbf{x}|\mathbf{y})$. The random walk, a Markov process, consists of randomly generated (Monte Carlo) test values of $\mathbf{x}$, represented in the vector $\hat{\mathbf{x}}$. The walk is guided by knowledge of the desired precipitation distribution $\mathbf{y}$, with uncertainty determined by $P(\mathbf{y}|\mathbf{x})$. Each test value of $\hat{\mathbf{x}}$, accompanied by a CM1 simulation, is referred to as an *iteration*; multiple iterations make up a Markov chain. In each MCMC iteration, the following steps are taken (flowchart shown in Fig. 3).

1. Candidate values for all parameters in $\hat{\mathbf{x}}$ are randomly drawn from a *proposal distribution* $q(\hat{\mathbf{x}}, \mathbf{x}_i)$ centered on the current set of parameters $\mathbf{x}_i$. The proposal distribution in this case is defined to be uncorrelated Gaussian, and the variance determines the size of perturbations to $\mathbf{x}_i$ in the Markov chain.
2. The CM1 model simulates a precipitation distribution $\hat{\mathbf{y}} = f(\hat{\mathbf{x}})$ using the new $\hat{\mathbf{x}}$ values, and the simulated precipitation distribution is compared with the desired distribution using the likelihood $P(\mathbf{y}|\mathbf{x})$. For a Gaussian likelihood,

$$P(\mathbf{y} \mid \hat{\mathbf{x}}) \propto \exp\left[-\frac{1}{2}(\mathbf{y}-\hat{\mathbf{y}})^T \Sigma_y^{-1}(\mathbf{y}-\hat{\mathbf{y}})\right] \quad (3)$$

where Σ_y is the precipitation error covariance matrix. In our case, we assume precipitation uncertainty is uncorrelated between regions, and as such Σ_y is a diagonal matrix of precipitation error variances.

3. The *acceptance ratio* (Tamminen and Kyrölä, 2001; Delle Monache et al. 2008; Posselt, 2013) determines whether the candidate $\hat{\mathbf{x}}$ will be accepted as a sample of the posterior probability distribution $P(\mathbf{x}|\mathbf{y})$. The acceptance ratio is defined as:

$$\rho(\mathbf{x}_i, \hat{\mathbf{x}}) = \frac{P(\hat{\mathbf{y}} \mid \hat{\mathbf{x}}) P(\hat{\mathbf{x}}) q(\hat{\mathbf{x}}, \mathbf{x}_i)}{P(\mathbf{y}_i \mid \mathbf{x}_i) P(\mathbf{x}_i) q(\mathbf{x}_i, \hat{\mathbf{x}})} \quad (4)$$

This is the ratio between the probabilities on the right hand side of Bayes' relationship for the candidate $\hat{\mathbf{x}}$ (numerator in (4)) and the current $\mathbf{x}_i$ (denominator in (4)). Since our proposal distribution is symmetric, $q(\mathbf{x}_i, \hat{\mathbf{x}}) = q(\hat{\mathbf{x}}, \mathbf{x}_i)$ and equation (4) reduces to the ratio of prior and likelihood distributions. In addition, since the prior is identical everywhere within the acceptable parameter ranges, equation (4) depends only on the ratio of likelihoods.

4. If the candidate $\hat{\mathbf{x}}$ produces a better fit to the desired precipitation distribution than $\mathbf{x}_i$ ($\rho > 1$), $\hat{\mathbf{x}}$ is *accepted*, or saved, as a sample in the Markov chain ($\mathbf{x}_{i+1} = \hat{\mathbf{x}}$). If the candidate $\hat{\mathbf{x}}$ does not produce an improved fit ($\rho < 1$), a test value is drawn from a Uniform (0,1) distribution. If this test value is less than the acceptance ratio, the candidate $\hat{\mathbf{x}}$ is saved as a sample in the Markov chain (this is termed *probabilistic acceptance*); if not, it is *rejected*, $\mathbf{x}_i$ is stored as another sample, and new candidate $\hat{\mathbf{x}}$ values are drawn.

The coin-flip style comparison between the acceptance ratio and a Uniform random variable used in the probabilistic acceptance procedure allows the algorithm to preferentially sample high-probability regions of posterior parameter space, avoid very low probability regions, and appropriately sample the parameter space in between. Altogether, the MCMC-generated sample of the posterior probability completely characterizes the solution to Eq. (2). Sequential iterations of the MCMC process constitute a *Markov chain*, and the MCMC algorithm may be constructed to use multiple chains to explore the parameter space. This study employed 15 chains, and the MCMC algorithm is similar to those described in Delle Monache et al. (2008), Posselt and Vukicevic (2010), Posselt and Bishop (2012), and Posselt et al. (2014).

The parameters **x** that define the control case in this study are associated with the thermodynamic profile given in Fig. 2, and produce a moderate amount of orographic precipitation concentrated on the windward slope (Fig. 4a). Precipitation reaches an approximately steady state a few hours into the simulation (Fig. 4b). Parameter ranges were chosen to encompass a variety of thermodynamic and wind profiles and mountain geometries. The orographic Froude numbers (defined as $Fr = \frac{\bar{u}}{N_m H_{mtn}}$, Baines (1995), sec. 1.4) associated with each sample in the Markov chains range from positive values near zero, some of which are associated with blocked flow in the model, to values on the order of 50, associated with cases of small amplitude, slow-moving gravity waves.

3. Results

3.1 One- and Two-Parameter Perturbation Experiments

Our ultimate goal is to determine which combinations of parameter values yield similar precipitation distributions as the control case, as well as to identify sensitivity and rapid transitions in the system. As mentioned above, this requires simultaneous perturbation of all six input parameters using the MCMC algorithm. Prior to performing such a study, it is useful to conduct a simplified analysis without using the MCMC algorithm, in which only one or two parameters are varied at a time and the rest held constant. This one- or two-at-a-time sensitivity analysis provides an initial estimate of the sensitivity of precipitation rate to changes in the control variables. As our focus is on upslope precipitation, we examine how precipitation rate in regions 2 and 3 (upwind slope; Fig. 1) changes with variation in each of the six parameters.

The slope of the precipitation rate *response function* (Fig. 5) indicates the degree of sensitivity to parameter changes: a steeper slope for a given change in a parameter reflects larger sensitivity to changes in that parameter. In addition to the response function slope, monotonicity and smoothness are important indicators of the parameter-precipitation rate relationship. A *non-monotonic* response, in which precipitation rate first increases with increasing parameter value, then decreases (or vice versa) at larger parameter values, means that scenarios exist in which two different parameter values will produce the same precipitation rate. A non-monotonic response also indicates a *non-unique* relationship between parameter and model output. A *non-smooth* response function, in which the model response changes suddenly around a particular parameter value or set of values, indicates the system experiences a rapid transition to a new state as the parameter increases beyond this value.

Examination of the response functions depicted in Fig. 5 reveals a range of behaviors in the model, from smooth, monotonic behavior to non-monotonic, non-smooth behavior. Precipitation rate increases monotonically with mountain height (Fig. 5a) in region 2 over the whole range of H_{mtn}, and in region 3 up to a mountain height of about 2.5 km. The non-monotonic change in precipitation rate with increasing mountain width (Fig. 5b) is due to the change in slope. As mountain width increases from 0 m, forced ascent occurs over a larger spatial region, leading to greater precipitation rate. However, as the width continues to increase with a fixed height, the slope decreases, resulting in smaller upward vertical motion and smaller precipitation rates. At large widths, precipitation rates are small and rain falls primarily downstream of the peak.

In general, the rain rate changes in a predictable and monotonic fashion with changes to the relative humidity (Fig. 5c): greater water vapor content leads to greater precipitation rate. Precipitation rates in region 3 exhibit a slight decrease at RH values greater than 95%, perhaps due to the fact that cloud and rain form farther upstream in an atmosphere with larger water vapor content. Surface potential temperature (Fig. 5d) increases result in an approximately monotonic increase in precipitation rate in both upwind slope regions. If relative humidity is held constant as temperature increases, the atmospheric water vapor content will increase. As such, the precipitation response to warming of the profile is similar to the response to increases in RH. Precipitation rate response to moist stability (Fig. 5e) is non-monotonic, first increasing then decreasing. As stability increases past 4×10^{-5} s^{-2}, the increased resistance to vertical motion suppresses precipitation. Above a moist stability value of approximately 1.05×10^{-4} s^{-2}, precipitation does not occur. Examination of the model output indicates that, at these values, stagnation occurs at the upwind slope and a back-propagating gravity wave suppresses cloud formation (as in MR05; Muraki and Rotunno 2013).

Increases in wind speed (Fig. 5f) from 1 to ~15 m s^{-1} result in increases in precipitation rate on the upwind slope (region 2, Fig. 1) and mountain top (region 3, Fig. 1). However, as wind speed increases beyond 15 m s^{-1}, precipitation rate concentrates increasingly at the mountain top with less on the upwind slope. This is consistent with advection of condensate farther downstream: for a given environment and mountain geometry, larger wind advects precipitation farther downstream, producing greater rainfall in region 3 at the expense of region 2. Interestingly, precipitation rate in both regions 2 and 3 plummets at wind speeds of 23 and 24 m s^{-1}, respectively, before rapidly increasing again. This behavior is closely related to the properties of mountain wave breaking, and will be discussed in more detail later.

In addition to one-at-a-time analyses, we can examine the joint response of two variables at a time by holding four of the six parameters constant at their control values, while varying the other two parameters incrementally across their defined ranges. In these experiments, the CM1 model was run for every combination of the two variable parameters, and the probability that the CM1 model output was equal to the control precipitation was then calculated for each parameter combination. As mentioned above, we assume the prior probability $P(\mathbf{x})$ is Uniform over the range of parameter values, and the precipitation rate likelihood $P(\mathbf{y}|\mathbf{x})$ is Gaussian with 2 mm hr^{-1} standard deviation. Direct computation of the PDFs that result from multiplying the prior and likelihood leads to a non-normalized solution to Bayes' Eq. (2). Probabilities may be displayed as two-dimensional *joint parameter probability density functions (PDFs)* that graphically display the conditional probability $P(\mathbf{x}|\mathbf{y})$. It is worth noting here that the two-parameter experiments already present a more comprehensive view of the orographic precipitation system and its sensitivity than previous modeling experiments. MR10 used the CM1 to conduct 79 experiments, the highest number found in our search of the literature; a single two-parameter PDF computation experiment includes 400 individual CM1 experiments (20 bins for each parameter).

Shown in Fig. 6 are three two-dimensional parameter PDFs from a set of three two-parameter experiments. In Fig. 6a, mean wind speed and stability, in the form of squared Brunt-Väisälä frequency, were varied while surface potential temperature, relative humidity, and mountain height and half-width were held constant at their control values. The control value for each varied parameter is indicated on the plots with a red line. The other plots follow a similar convention; Fig. 6b shows variations in potential temperature and RH, while Fig. 6c shows variations in mountain height and half-width. Brightest colors indicate the highest probability that the combination of parameters at that point produced a precipitation rate and distribution similar to the control distribution.

A first look shows a well-defined high-probability mode in wind speed and stability (Fig. 6a), centered about the control values; precipitation rate output from the model is highly sensitive to changes in these parameters. In addition to a narrowly defined high probability region near the control values of N_m^2 and $\bar{u}$, a tail of high probability extends to high wind speeds at low stability values. Wind speed is positively correlated with stability (and vice versa): increases in wind speed lead to increases in precipitation rate that may be compensated for by increasing the resistance to vertical motion (via an increase in stability). The model response to changes in relative humidity and surface potential temperature (Fig. 6b) has a large probability spread and diffuse gradients. At temperatures of 285-295 K, a decrease in RH, or available moisture, can compensate for increases in θ_{sfc} that may lead to larger precipitation rates. Above 295 K, however, the model instead develops a greater sensitivity to changes in RH and a reduced sensitivity to changes in θ_{sfc}. Mountain height and half-width (Fig. 6c) display a well-defined high-probability mode, but lack the correlation seen in wind speed and stability. High probability exists for a roughly rectangular region bounded by mountain height and half-width values; only parameter values similar to control values produce precipitation rates similar to control precipitation.

3.2 MCMC-Based Orographic Precipitation Analysis

While one- and two-parameter experiments yield information about the system and its complex relationships, a complete analysis of the combinations of parameters that produce a given rainfall distribution requires simultaneous perturbation of all six parameters. Such an exercise is intractable for more than a few parameters if it is done by brute force. As mentioned above, the question of which parameter values produce a given distribution of precipitation, and the associated sensitivities, can be addressed using Bayesian analysis via application of an MCMC algorithm. Early analysis of output from the MCMC algorithm indicated that approximately 100,000 simulations were sufficient to capture the salient properties of the parameter probability distribution. Although Haario et al. (1999) suggested only 20,000 samples were required to sample a multivariate 8-dimensional Gaussian distribution, we ran the MCMC experiment until it had produced more than one million runs of the CM1 model. The results comprise a thorough statistical sample that spans the complicated posterior distribution shown by univariate and bivariate sensitivity experiments, as well as a rich repository of model output for further analysis. We computed the R-statistic ($\hat{R}$, Gelman et al. 2004), comparing within-chain variance to between-chain variance, to diagnose whether the 15 MCMC chains converged to sampling a stationary posterior distribution. A value of $\hat{R} < 1.1$ for each parameter generally indicates sufficient mixing and convergence. As shown in Fig. 7, all parameters exhibit $\hat{R} < 1.1$ after about 40,000 samples per chain, and $\hat{R} \leq 1.05$ by the time sampling ends.

MCMC produces a posterior probability distribution with variability in all 6 parameter dimensions. Because it is challenging to visualize a 6-dimensional space, we present the PDF obtained from MCMC in the form of 2-dimensional marginal probability distributions for each pair of parameters (Fig. 8). Probabilities displayed in each 2-dimensional plot have been integrated over the other 4 dimensions, which may cause the highest probability regions to center on parameter combinations other than the control values. Parameter sets that produced precipitation rates close to those in the control simulation are associated with the largest probabilities. The degree of sensitivity of precipitation rate to a change in parameter can be determined via the gradient in probability, as well as the extent of the probability maximum/maxima. A sharp gradient in probability means that a small change in a parameter value produces a large change in precipitation rate; a small probability maximum indicates there are relatively few parameter values that produce precipitation rates close to what was observed (in this case, what was produced by the control simulation).

Precipitation rates consistent with the control simulation occur with nearly equal probability for a large range of RH values. Conversely, the model expresses the greatest precipitation rate sensitivity to mean wind speed, static stability, and mountain geometry, as reflected in the well-defined modes and small probability dispersion. Taller orography and steeper slopes impede moist ascent, and as impediments become larger, stability and latent heating become increasingly important influences on the properties of the forced ascent. In addition, wind speed, stability, and the depth of air being lifted all affect hydrometeor growth, and location and amount of precipitation reaching the ground. Blocking or stagnation upwind of the mountain may result in convergence and precipitation upstream. However, if air parcels move too quickly, clouds may encounter leeward subsidence before precipitation has the chance to fall (Sawyer 1956; Smith 1979, 2006).

These plots also highlight parameter inter-relationships. The most distinct relationships are between stability, mean wind speed, and mountain geometry. Notable correlations are evident in the 2D covariance between mean wind speed and stability (Fig. 8a); wind speed and mountain height (Fig. 8g); wind speed and half-width (Fig. 8k); and height and half-width (Fig.

8o). An increase in mean wind speed is positively correlated with an increase in stability, and the same can be said for mean wind speed and width. Therefore, increasing the stability (making air less susceptible to ascent) and increasing the mountain width (resulting in a shallower slope) can compensate for increases in wind speed that cause higher precipitation rates. On the other hand, increases in wind speed are negatively correlated with increases in mountain height. The same relationship exists between mountain height and half-width. Decreasing mountain height and reducing the amount of lift provided by terrain may compensate for larger precipitation rates caused by increasing wind speed. Increasing precipitation rate by making a taller mountain can be tempered by decreasing the half-width; the steeper slope may induce blocking or may favor the advection of rainfall on the downslope and decrease the precipitation amount upstream.

At first glance, it seems that a precipitation rate increase due to increasing temperature may be stemmed by decreasing the stability. However, upon closer inspection, the MCMC experiment reveals a complex multimodal probability structure in the surface potential temperature and stability PDF (Fig. 8c), indicating that multiple discrete combinations of surface potential temperature and stability produce the same precipitation rates. There are two distinct probability modes: one warmer and more stable (corresponding to the control simulation) and one cooler and less stable (283 K, 2×10^{-5} s^{-2}). A warmer atmosphere requires a stronger aversion to rising motion in order to produce the same amount of precipitation as a cooler atmosphere. Surface potential temperature and stability are not the only parameters that exhibit multimodality; prominent secondary probability modes can be seen in the marginal probability distributions of surface potential temperature and stability (Fig. 8c), stability and RH (Fig. 8e), and surface potential temperature and RH (Fig. 8f).

4. Discussion

From our one- and two-parameter sensitivity tests, as well as output from the MCMC experiment, we ascertain that precipitation rate has a complex dependence on changes in the control parameters: the overall response is rarely linear, and is at times non-smooth or non-monotonic. In the process of running the MCMC algorithm, output data from CM1 model simulations corresponding to each MCMC iteration were stored. This database of simulated output can be used to examine the physics that give rise to the probability structures in the MCMC output.

In our one-parameter sensitivity experiments, we noted that precipitation rate in regions 2 and 3 exhibited abrupt shifts when mean wind speed (Fig. 5f) was changed from 20-25 m/s with all other parameters held constant. Using the database of simulated output described above, we may compare model output from our control case to model output with the same input parameters, except for increased wind speed. Fig. 9 depicts model output from the last hour of simulation for our control case (Figs. 9a,b), as well as for cases with the same input parameters but with higher wind speeds: 20 m/s (Figs. 9c,d), 21 m/s (Figs. 9e,f), 22 m/s (Figs. 9g,h), 23 m/s (Figs. 9i,j), 24 m/s (Figs. 9k,l), and 25 m/s (Figs. 9m,n). The left column depicts vertical cross sections of the flow and cloud distribution at the last hour of simulation (as in Fig. 4a), and the right column contains Hovmöller diagrams of rain rate for the entire simulation (as in Fig. 4b). For figures in the left column, recall that the thick black line outlines liquid precipitation, and the gray shading indicates the presence of cloud.

Recall from our analysis of Fig. 5f that the precipitation rate on the upwind slope (region 2) generally increases with increasing wind speed until about 20 m/s, decreases rapidly until 23 m/s, and increases dramatically again after. The upwind side of the top of the mountain (region 3) exhibits a similar response; precipitation rate increases until 22 m/s, decreases rapidly, and starts increasing again at 25 m/s. The Hovmöller diagrams in Fig. 9 show ever-increasing precipitation rates on the upwind slope of the mountain. A close examination of the vertical cross-sections, however, shows that, for wind speeds of 20-23 m/s, increasing wind speeds result in more surface precipitation near the mountain top, reducing the precipitation rate in region 2. A change occurs when wind speeds reach 24 m/s; surface precipitation spreads out again along the upwind slope, returning precipitation to region 2 at the expense of region 3. It is at this wind speed that the precipitation distribution closely resembles that of the control case. As wind speeds continue to increase to 25 m/s and beyond, precipitation rate increases as it did before.

It is notable that, while the precipitation distribution at $\bar{u}$ = 24 m/s was similar to that of the control case (with $\bar{u}$ = 13 m/s), the flow and cloud distribution in the higher wind case were entirely different, exhibiting a pronounced downstream breaking mountain wave. This indicates the possibility of two (or more) distinct sets of solutions that produce similar precipitation in very different atmospheres. We noted in the MCMC results two distinct high probability modes were evident in the marginal PDF of θ_{sfc} and stability (Fig. 8c). The first mode corresponds to our control case, defined by the parameter values listed in Table 1. Fig. 10a displays a vertical cross section at the last hour of the control simulation, as in Fig. 4a. Wind speed increases as air flows down the lee slope of the mountain, and a small amplitude mountain wave is evident above the mountain peak. The second high-probability mode has the following combination of parameter values: mean wind speed is 17 m s^{-1}, squared Brunt-Väisälä frequency is $2x10^{-5}$ s^{-2}, surface potential temperature is 283 K, relative humidity is 95%, mountain height is 2.75 km, and mountain half-width is 20 km. A vertical cross-section at the last hour of the high-probability mode simulation is presented in Fig. 10b. While liquid precipitation reaches the surface in approximately the same location as in the control case, similarities to the control case end there.

The high-probability mode exhibits a large upstream cloud shield and an intense downslope wind storm. A breaking mountain wave propagates vertically downstream of the mountain top, and another tongue of narrow swath of precipitation reaches nearly to the ground far upstream. While leeside effects of this magnitude are uncommon, and likely exaggerated due to necessary model simplifications, they are meteorologically relevant (Seibert 1990, Zängl and Hornsteiner 2007).

In addition to examining the differences in atmospheric flow, cloud, and precipitation between the control case and a second high probability mode, it is useful to explore whether the atmosphere associated with the second high-probability mode exhibits similar sensitivity to changes in profile and mountain shape. To do this, we conduct two-parameter perturbation experiments identical to those described in section 3.1, but with the modal parameter values described in the previous paragraph used as the baseline instead of our control case parameters. Figs. 11a-c (top row) recall the 2D PDFs from the control case, whereas Figs. 11d-f show the 2D PDFs from the second high-probability mode.

The high-probability mode PDFs take on a different probability structure than the PDFs from the control case. Multiple probability structures in wind speed and stability (Fig. 11d) are more defined and separated; on the other hand, the well-defined probability region in mountain height and half-width (Fig. 11f) has shrunk, implying an even greater sensitivity to those parameters. While the PDFs express nearly no sensitivity to relative humidity (Fig. 11e), there is a pronounced difference in potential temperature compared to the control case: potential temperature exhibits a distinctly bivariate probability structure. The atmospheric and probabilistic diversity between the control case and the second high-probability MCMC mode capture the complexity of this system—two distinct atmospheric soundings and mountain geometries with very different sensitivity structure produce nearly the same precipitation rate.

Finally, in addition to examining the bulk sensitivity and probability structure associated with changes in one or two parameters at a time, the computations performed in this study may be used to produce a first assessment of the required degree of accuracy for precipitation measurements. In essence, we seek to determine how accurate measurements must be to constrain the relationships between precipitation and input parameters. We do this by examining the change in parameter PDFs with changes in observational error. The error used in this study is Gaussian with a 2 mm hr^{-1} standard deviation (Figs. 12d-f, as in Fig. 6). Reducing the standard deviation by a factor of 0.5 to 1 mm hr^{-1} (Fig. 12a-c) leads to a contraction in high probability regions. Any secondary modes are still present, being produced by the physical behavior of the model itself. However, algorithms that search for a unique probability mode would now, with increased observation accuracy, likely find the true solution. Inflating the error, for example to standard deviation of 5 mm hr^{-1} (Figs. 12g-i), greatly expands regions with already high probability, and allows more mass in lower-probability regions. The result is an increase in non-uniqueness, or distinct multiple modes with equivalent (near unity) probability. This in effect lessens the significance of primary probability modes and makes convergence difficult for algorithms that search for a unique solution. As noted in Posselt et al. (2008) and Posselt and Vukicevic (2010), adding information to observations by reducing the observation error does not change the functional response of model output to changes in the input: the probability structure is the same. However, our results indicate that increasing observation accuracy to 1 mm hr^{-1} would have, in this case, produced a clearly dominant solution.

5. Summary and Conclusions

Although the dynamics of orographic precipitation have been a focus of study for many years, recent terrain-induced flooding in highly populated areas highlight the necessity of advancement in scientific understanding of the orographic precipitation system. Orographic precipitation occurs in many and varied flow regimes; our current study focuses on a moist stable to moist neutral idealized scenario. In order to answer questions concerning the sensitivity of topographically forced precipitation to environmental and mountain characteristics, we employed the CM1 cloud-resolving model in conjunction with a Markov Chain Monte Carlo algorithm. MCMC allows us to sample a substantial parameter space in a thorough, robust, and (relative to brute force sensitivity analysis) computationally efficient manner, and the resulting joint parameter probability distribution can be used to identify relationships between parameters and observations, sources of model sensitivity, and the result of adjusting observation uncertainty. Our major conclusions from this work are as follows.

1. The orographic precipitation system has a *non-unique solution*. The same surface precipitation rate and distribution can be obtained with very different sounding, flow, and terrain characteristics. These different mountain geometry and sounding characteristics correspond to a secondary high-probability mode in the Bayesian posterior PDF, which has an entirely different cloud shield, mountain wave, and downslope wind than the control case.
2. Sensitivity tests conducted using a secondary high-probability mode resulted in a *different sensitivity profile* than the original control case. While all tests showed sensitivity to changes in wind speed and Brunt-Väisälä frequency, model sensitivity to changes in surface potential temperature (and even relative humidity) depends on the specific sounding and mountain geometry. Additionally, co-variability between wind speed and stability, as well as mountain height and half-width, does not depend on the control variables. Co-variability or relationship between temperature and relative humidity, however, is situation-dependent.

3. In certain flow regimes, the model displays *high sensitivity* to small changes in certain parameters, namely surface potential temperature and wind speed. A further examination of flow and thermodynamic structures in individual model runs shows that these small parameter changes lead to large alterations in moist mountain wave structure and the associated surface precipitation rate.
4. Finally, *changes in observation uncertainty* affect the ability to obtain a unique flow configuration from a given precipitation rate and distribution. Improving precipitation constraint from 2 mm hr^{-1} to 1 mm hr^{-1} produced a dominant solution. Degrading the accuracy to 5 mm hr^{-1}, on the other hand, results in a loss of that unique solution.

While this research comprehensively explores the parameter space associated with moist neutral orographic precipitation, we have not considered many of the key sources of variability that influence orographic precipitation. This was intentional, as the goal of this research was to extend previous univariate sensitivity studies into the multivariate domain, and to demonstrate the utility of Bayesian MCMC methods for exploring relationships in a physical system. Additional experiments could be performed to examine the sets of environmental and mountain geometry parameters consistent with precipitation rates concentrated on the mountain top and downwind slope, along with their canonical flow structures. For simplicity, we have utilized the simplest cloud microphysical parameterization available in the CM1. The details of cloud particle interactions, and in particular ice and mixed phase processes, have a strong influence on the characteristics of orographic precipitation for both warm and cold-based clouds. Changes to the cloud particle size distributions and assumed ice particle shape influence settling velocities and particle population interactions, and as such have a significant effect on precipitation rate and distribution. Posselt and Vukicevic (2010) used the MCMC algorithm to explore cloud microphysical sensitivity in simulations of deep convection, and we plan to conduct similar experiments for orographic precipitation cases.

Our mountain geometry was highly idealized, utilizing an infinite ridge with no along-ridge variability. In a stable flow regime, this configuration allows the use of quasi-2D simulations, as the flow will not vary with location in a non-convective environment. However, many studies of observed orographic rain and snowfall have shown that the presence of gaps in a barrier lead to concentration of the flow (so-called *gap winds*) that exert an influence on both the upwind and downwind precipitation via their influence on cross-mountain flow. We also neglected the influence of wind shear, changes in land use, the associated differences in sensible and latent heat flux, and surface friction, all of which may improve the physical realism of simulations in future study. We plan to expand our study to include unstable and convective precipitation cases, as in MR09, MR10, and Miglietta and Rotunno (2012, 2014), in addition to the moist stable and neutral cases represented here. Consideration of convective environments will greatly increase the complexity of our experiments, as previous research has clearly illustrated that three-dimensional domains and high horizontal grid spacing are required to realistically represent convective circulations.

Acknowledgements

The authors would like to acknowledge the National Center for Atmospheric Research Graduate Visitor Program and the Warner Internship for Scientific Enrichment for their generous support and guidance during the residence of Ms. Samantha Tushaus and Prof. Derek Posselt. We also thank Dr. George Bryan for his assistance with CM1. The comments of two anonymous reviewers served to greatly improve the presentation of our results. This work was supported by National Science Foundation Physical and Dynamic Meteorology grant AGS 1005454.

REFERENCES

Baines, P.G., 1995: *Topographic Effects in Stratified Flows*. Cambridge University Press, 482 pp.

Barcilon, A., J.C. Jusem, and P.G. Drazin, 1979: On the two- dimensional hydrostatic flow of a stream of moist air over a mountain ridge. *Geophys. Astrophys. Fluid Dyn*., **13**, 125– 140.

Bougeault, P., and Coauthors, 2001: The MAP Special Observing Period. *Bull. Amer. Meteor. Soc*., **82**, 433–462.

Bryan, G.H., and J.M. Fritsch, 2002: A benchmark simulation for moist nonhydrostatic numerical models. *Mon. Wea. Rev.*, **130**, 2917-2928.

Bryan, G.H., J.C. Wynguard, and J.M. Fritsch, 2003: Resolution requirements for the simulation of deep moist convection. *Mon. Wea. Rev.*, **131**, 2394-2416.

Buzzi, A., and L. Foschini, 2000: Mesoscale meteorological features associated with heavy precipitation in the Southern Alpine Region. *Meteor. Atmos. Phys*., **72**, 131–146.

Colle, B.A., 2004: Sensitivity of orographic precipitation to changing ambient conditions and terrain geometries: An idealized modeling perspective. *J. Atmos. Sci*., **61**, 588–606.

Deardorff, J.W., 1980: Stratocumulus-capped mixed layer derived from a three-dimensional model. *Bound. Layer. Meteor.*, **18**, 495-527.

Delle Monache, L., and Co-authors, 2008: Bayesian inference and Markov Chain Monte Carlo to reconstruct a contaminant source at continental scale. *J. Appl. Meteor. Climatol.*, **47**, 2600-2613.

Doswell, C.A., III, C. Ramis, R. Romero, and S. Alonso, 1998: A diagnostic study of three heavy precipitation episodes in the western Mediterranean. *Wea. Forecasting*, **13**, 102–124.

Douglas, C.K.M., and J. Glasspoole, 1947: Meteorological conditions in orographic rainfall in the British Isles. *Q.J.R. Meteor. Soc*., **73**, 11–38.

Durran, D. R., and J. B. Klemp, 1982: The effects of moisture on trapped lee waves. *J. Atmos. Sci*., **39**, 2490–2506.

Durran, D. R., and J. B. Klemp, 1983: A compressible model for the simulation of moist mountain waves. *Mon. Wea. Rev*., **111**, 2341–2361.

Gelman, A., J.B. Carlin, H.S. Stern, and D.B. Rubin, 2004: *Bayesian Data Analysis,* 2nd ed. Chapman and Hall/CRC, 696 pp.

Haario, H., E. Saksman, and J. Tamminen, 1999: Adaptive proposal distribution for random walk Metropolis algorithm. *Comp. Stat.*, **14**, 375-395.

Kessler, E., 1969: On the distribution and continuity of water substance in atmospheric circulations. *Meteorol. Monogr.*, No. 32, Amer. Meteor. Soc., Boston, 84 pp.

Kingsmill, D., and co-authors, 2006: Overview of the Sierra Hydrometeorology Atmospheric River Experiment (SHARE). *12th Conf. on Mountain Meteorology*, Santa Fe, NM, Amer. Meteor. Soc., P1.1.

Miglietta, M.M., and A. Buzzi, 2001: A numerical study of moist stratified flows over isolated topography. *Tellus*, **53A**, 481– 499.

Miglietta, M.M., and R. Rotunno, 2005: Simulations of Moist Nearly Neutral Flow over a Ridge. *J. Atmos. Sci.*, **62**, 1410–1427.

Miglietta, M.M., and R. Rotunno, 2006: Further Results on Moist Nearly Neutral Flow over a Ridge. *J. Atmos. Sci.*, **63**, 2881–2897.

Miglietta, M.M., and R. Rotunno, 2009: Numerical Simulations of Conditionally Unstable Flows over a Mountain Ridge. *J. Atmos. Sci.*, **66**, 1865–1885.

Miglietta, M.M., and R. Rotunno, 2010: Numerical Simulations of Low-CAPE Flows over a Mountain Ridge. *J. Atmos. Sci.*, **67**, 2391–2401.

Miglietta, M. M., and R. Rotunno, 2012: Application of theory to observed cases of orographically forced convective rainfall, *Mon. Wea. Rev*., **140**, 3039-3053.

Miglietta, M. M., and R. Rotunno, 2014: Numerical simulations of sheared conditionally unstable flows over a mountain ridge, *Mon. Wea. Rev*., In Press.

Muraki, D.J., and R. Rotunno, 2013: Internal Gravity Waves in a Saturated Moist Neutral Atmosphere. *J. Amost. Sci.*, **70**, 3693-3709.

Neiman, P.J., F.M. Ralph, A.B. White, D.E. Kingsmill, P.O.G. Persson, 2002: The Statistical Relationship between Upslope Flow and Rainfall in California's Coastal Mountains: Observations during CALJET. *Mon. Wea. Rev.*, **130**, 1468–1492.

Neiman P. J., L.J. Schick, F.M. Ralph, M. Hughes and G.A. Wick, 2011: Flooding in western Washington: The connection to atmospheric rivers. *J. Hydrometeor*., **12**, 1337-1358.

Posselt, D.J., T.S. L'Ecuyer, and G.L. Stephens, 2008: Exploring the Error Characteristics of Thin Ice Cloud Property Retrievals Using a Markov Chain Monte Carlo Algorithm. *Geophys. Res. Lett.*, **113**, D24206.

Posselt, D.J., and T. Vukicevic, 2010: Robust Characterization of Model Physics Uncertainty for Simulations of Deep Moist Convection. *Mon. Wea. Rev.*, **138**, 1513-1535.

Posselt, D.J., and C.H. Bishop, 2012: Nonlinear parameter estimation: Comparison of an Ensemble Kalman Smoother with a Markov Chain Monte Carlo algorithm. *Mon. Wea. Rev.*, **140**, 1957-1974.

Posselt, D.J., 2013: Markov Chain Monte Carlo Methods. *Theory and Applications in Data Assimilation for Atmospheric, Oceanic and Hydrologic Applications Vol. II*, S. K. Park and L. Xu, Eds., Springer, 59-87.

Posselt, D.J.**,** D. Hodyss, and C.H. Bishop, 2014: Errors in Ensemble Kalman Smoother Estimates of Cloud Microphysical Parameters. Mon. Wea. Rev., **142,** 1631-1654.

Ralph F. M., P.J. Neiman, and G.A. Wick. 2004. Satellite and CALJET aircraft observations of atmospheric rivers over the eastern North Pacific ocean during the winter of 1997/98. *Mon. Wea. Rev*., **132**, 1721 – 1745.

Ralph, F.M., P.J. Nieman, and R. Rotunno, 2005: Dropsonde observations in low-level jets over the northeastern Pacific Ocean from CALJET-1998 and PACJET-2001: Mean vertical-profile and atmospheric-river characteristics. *Mon. Wea. Rev*., **133**, 889–910.

Ralph, F.M., and M.D. Dettinger, 2011: Storms, Floods, and the Science of Atmospheric Rivers. EOS, Transactions, *Amer. Geophys. Union*, **92**, 265-266.

Rotunno, R. and R. Ferretti, 2003: Orographic effects on rainfall in MAP cases IOP 2b and IOP 8. *Q.J.R. Meteor. Soc*., **129**, 373–390.

Rotunno, R. and R.A. Houze, 2007: Lessons on orographic precipitation from the Mesoscale Alpine Programme. *Q.J.R. Meteor. Soc.*, **133**, 811–830.

Rutz, J.J., W.J. Steenburgh, and F.M. Ralph, 2014: Climatological Characteristics of Atmospheric Rivers and Their Inland Penetration over the Western United States. *Mon. Wea. Rev.*, **142**, 905-921.

Sarker, R.P., 1967: Some modifications in a dynamical model of orographic rainfall. *Mon. Wea. Rev*., **95**, 673–684.

Sawyer, J.S., 1956: The physical and dynamical problems of orographic rain. *Wea.*, **11**, 375-381.

Schultz, D. M., and Co-authors, 2002: Understanding Utah Winter Storms: The Intermountain Precipitation Experiment. *Bull. Amer. Meteor. Soc.*, **83**, 189-210.

Seibert, P., 1990: South Foehn Studies Since the ALPEX Experiment. *Meteor. Atmos. Phys.,* **43**, 91-103.

Smith, R.B., 1979: The influence of mountains on the atmosphere. *Advances in Geophysics Vol. 21*, B. Saltzman, Ed., Academic Press, 87-230.

Smith, R.B., 2006: Progress on the theory of orographic precipitation. *GSA Spec. Pap.*, **398**, 1-16.

Stoelinga, M.T., and co-authors, 2003: Improvement of Microphysical Parameterization Through Observational Verification Experiment. *Bull. Am. Meteor. Soc.*, **84**, 1807-1826.

Tamminen, J., and E. Kyrölä, 2001: Bayesian solution for nonlinear and non-Gaussian inverse problems by Markov Chain Monte Carlo method. *J. Geophys. Res.*, **106**, 14377-14390.

Vukicevic, T., and D. J. Posselt, 2008: Analysis of the Impact of Model Nonlinearities in Inverse Problem Solving. *J. Atmos. Sci*., **65**, 2803-2823.

Zängl, G., and M. Hornsteiner, 2007: The exceptional Alpine south foehn event of 14-16 November 2002: a case study. *Meteor. Atmos. Phys.*, **98**, 217-238.

List of Tables

Table 1. Maximum and minimum values for all model input parameters, as well as value of each parameter used in control case.

Parameter Description	Control	Min	Max	Symbol	Units
Mean wind speed	13	2	30	$\bar{u}$	m s^{-1}
Squared, Moist Brunt-Väisälä frequency	$4x10^{-5}$	$2.5x10^{-6}$	$2x10^{-4}$	N_m^2	s^{-2}
Surface potential temperature	292	280	300	θ_{sfc}	K
Relative humidity	0.95	0.8	1.0	RH	none
Mountain height	$2.35x10^3$	$3x10^2$	$3x10^3$	H_{mtn}	m
Mountain half-width	$3x10^4$	$5x10^3$	$1x10^5$	W_{mtn}	m

Table 2. Precipitation rate averaged over each precipitation region on the mountain during the last hour of simulation in the control run.

	Region 1	**Region 2**	**Region 3**	**Region 4**	**Region 5**	**Region 6**
Averaged Precipitation Rate (mm hr^{-1})	2.70	5.49	7.74	1.87	$1.13x10^{-2}$	0.0

List of Figures

1. Visual depiction of the case study topography and the six precipitation bins.

2. Modeled skew-T diagram from CM1 depicting the atmosphere entering the westernmost (upwind) edge of the domain during the first hour in the control case. Wind speed is in units of m s^{-1}.

3. *(a)* X-Z cross-section of model domain during last hour of simulation. Cloud liquid water content shaded in gray: $0.01 < q_c < 0.1$ g kg^{-1} in light grey, $0.1 < q_c < 0.5$ g kg^{-1} in medium grey, and $q_c > 0.5$ g kg^{-1} in dark grey. Thick black contours outline regions of liquid precipitation greater than 0.2 g kg^{-1}. *U*- and *w*-direction streamlines are colored by *u*- wind component (m s^{-1}). *(b)* Hovmöller diagram of precipitation rate (mm hr^{-1}, shaded). Rain rate greater than 0.2 mm hr^{-1} contoured in black.

4. Flowchart illustrating the Markov chain Monte Carlo process.

5. Response of precipitation (mm hr^{-1}) to changes in each of the model input parameters. Red lines indicate the parameter value used in the control case. The solid line represents precipitation response in precipitation region 2 on the mountain, and the dashed line shows the response for precipitation region 3.

6. Two-dimensional joint PDFs of (*a*) wind speed and stability, (*b*) surface potential temperature and relative humidity, and (*c*) mountain height and half-width from a parameter perturbation experiment. Red lines indicate the parameter value used in the control case. Bright colors at any point imply a high probability that the parameter combination at that point produced precipitation output similar to the control output.

7. R-statistic ($\hat{R}$) values for each model input parameter, for successively greater numbers of samples.

8. Posterior two-dimensional marginal PDFs for all pairs of input parameters from the MCMC experiment. As in Fig. 5, red lines indicate the parameter value used in the control case. White solid and dashed lines contour the 68% and 95% probability mass, respectively. Bright colors at any point imply a high probability that the parameter combination at that point produced precipitation output similar to the control output.

9. Contours, shading, and colors as in Fig. 3. X-Z cross-sections of the model domain during last hour of simulation (*first column*). Hovmöller diagrams of precipitation rate (*second column*). Each row represents model output for varying wind speeds: 13 m s^{-1} (control case; *a*,*b*), 20 m s^{-1} (*c*,*d*), 21 m s^{-1} (*e*,*f*), 22 m s^{-1} (*g*,*h*), 23 m s^{-1} (*i*,*j*), 24 m s^{-1} (*k*,*l*), and 25 m s^{-1} (*m*,*n*).

10. Contours, shading, and colors as in Fig. 3a. *(a)* X-Z cross-section of control case. *(b)* X-Z cross-section of the second MCMC high-probability mode, as described in Section 4.

11. Contours, lines, and shading as in Fig. 5. The *first column* contains 2D joint PDFs of wind speed and stability; the *second column* contains 2D PDFs of surface potential

temperature and relative humidity; and the *third column* contains 2D PDFs of mountain height and half-width. The *first row* represents the control case; the *second row* represents the second MCMC high-probability mode.

12. Contours, lines, and shading as in Fig. 5. The *first column* contains 2D joint PDFs of wind speed and stability; the *second column* contains 2D PDFs of surface potential temperature and relative humidity; and the *third column* contains 2D PDFs of mountain height and half-width. The *first row* represents the control case with 1σ error; the *second row* represents the control case with 2σ error; and the *third row* represents the control case with 5σ error.

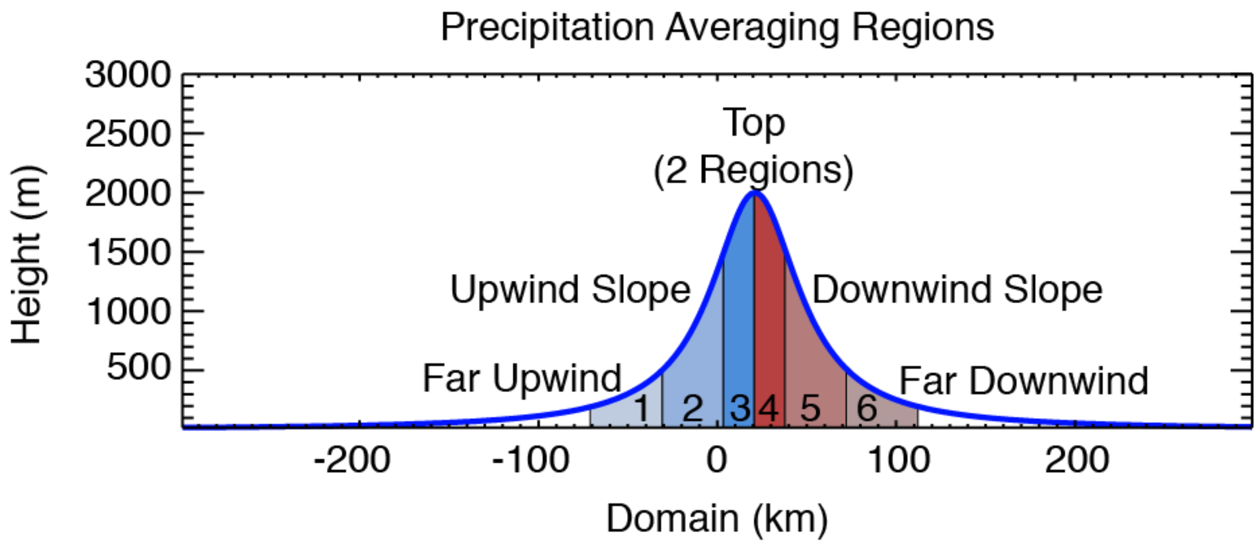

Figure 1. Visual depiction of the case study topography and the six precipitation bins.

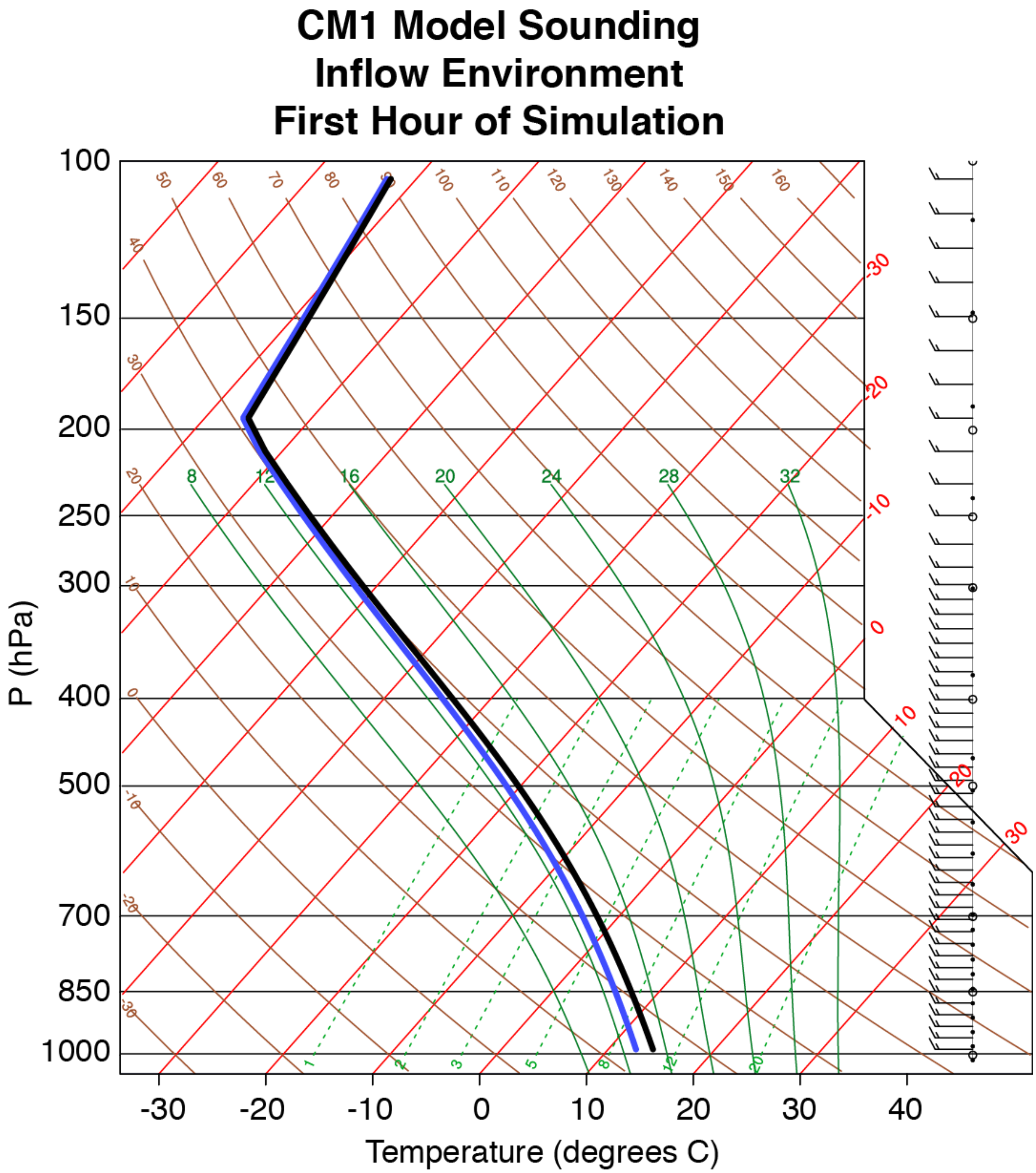

Figure 2. Modeled skew-T diagram from CM1 depicting the atmosphere entering the westernmost (upwind) edge of the domain during the first hour in the control case. Wind speed is in units of m s^{-1}.

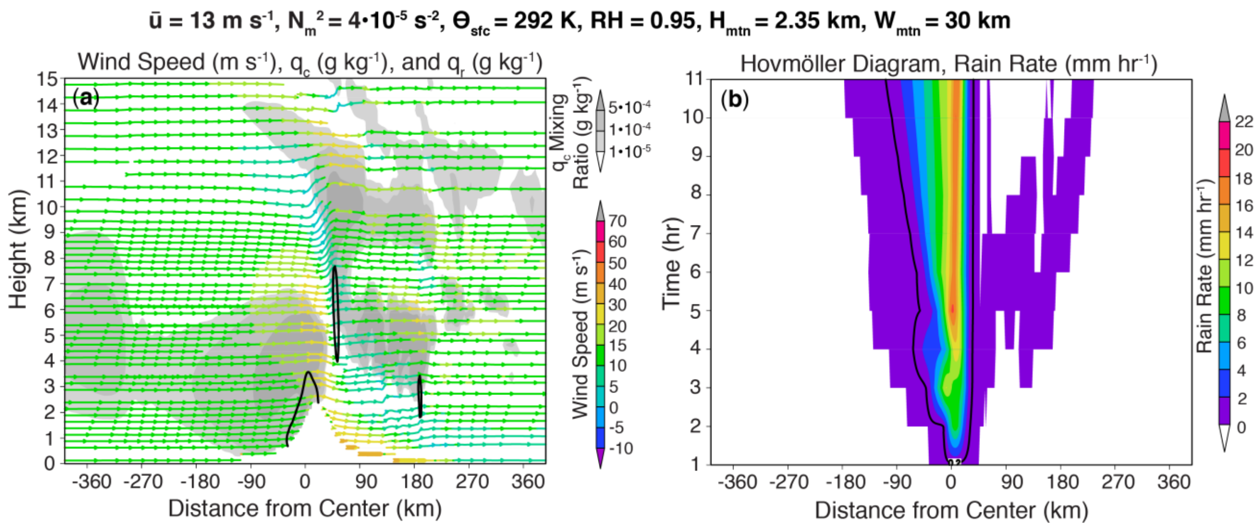

Figure 3. *(a)* X-Z cross-section of model domain during last hour of simulation. Cloud liquid water content shaded in gray: $0.01 < q_c < 0.1$ g kg^{-1} in light grey, $0.1 < q_c < 0.5$ g kg^{-1} in medium grey, and $q_c > 0.5$ g kg^{-1} in dark grey. Thick black contours outline regions of liquid precipitation greater than 0.2 g kg^{-1}. *U*- and *w*-direction streamlines are colored by *u*- wind component (m s^{-1}). *(b)* Hovmöller diagram of precipitation rate (mm hr^{-1}, shaded). Rain rate greater than 0.2 mm hr^{-1} contoured in black.

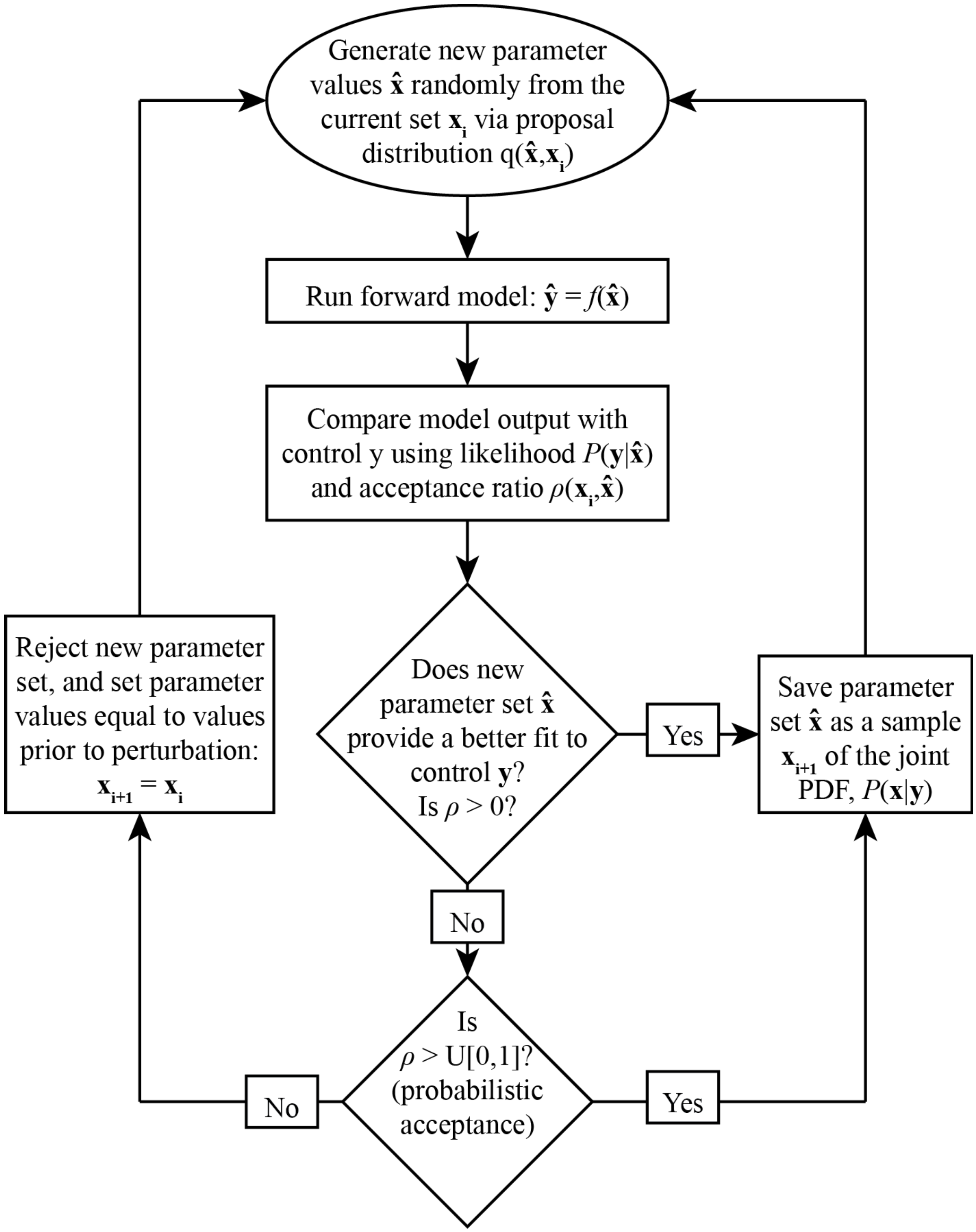

Figure 4. Flowchart illustrating the Markov chain Monte Carlo process.

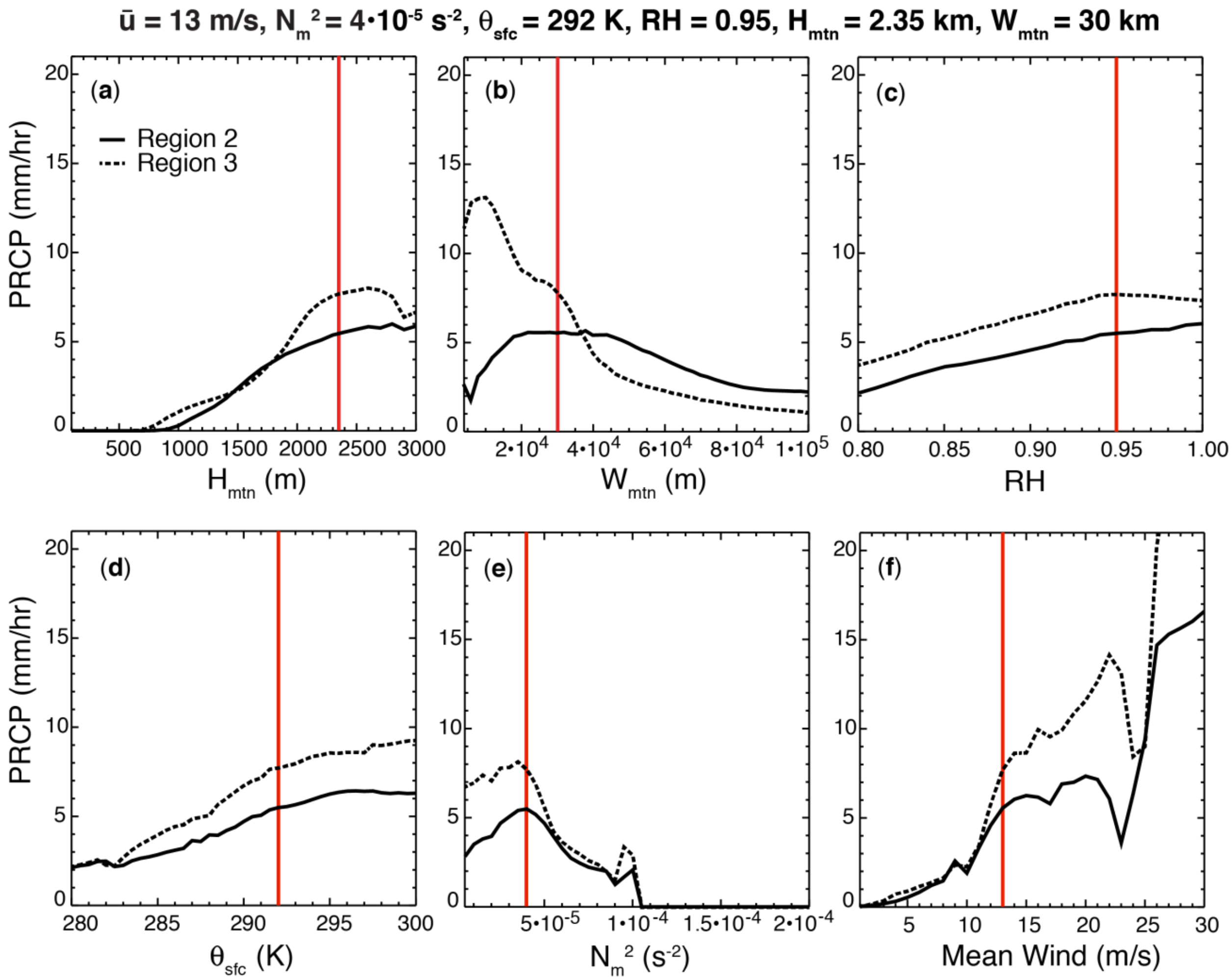

Figure 5. Response of precipitation (mm hr^{-1}) to changes in each of the model input parameters. Red lines indicate the parameter value used in the control case. The solid line represents precipitation response in precipitation region 2 on the mountain, and the dashed line shows the response for precipitation region 3.

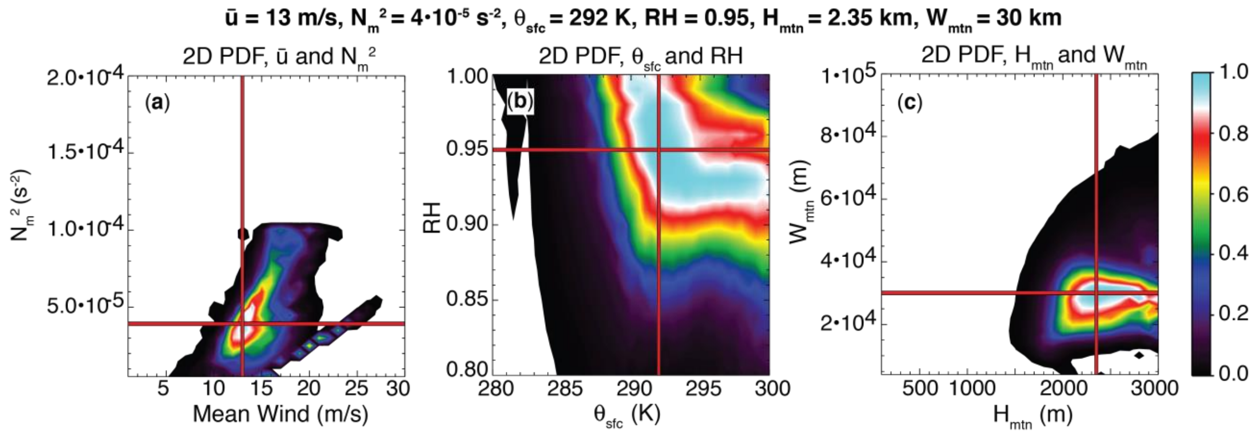

Figure 6. Two-dimensional joint PDFs of (*a*) wind speed and stability, (*b*) surface potential temperature and relative humidity, and (*c*) mountain height and half-width from a parameter perturbation experiment. Red lines indicate the parameter value used in the control case. Bright colors at any point imply a high probability that the parameter combination at that point produced precipitation output similar to the control output.

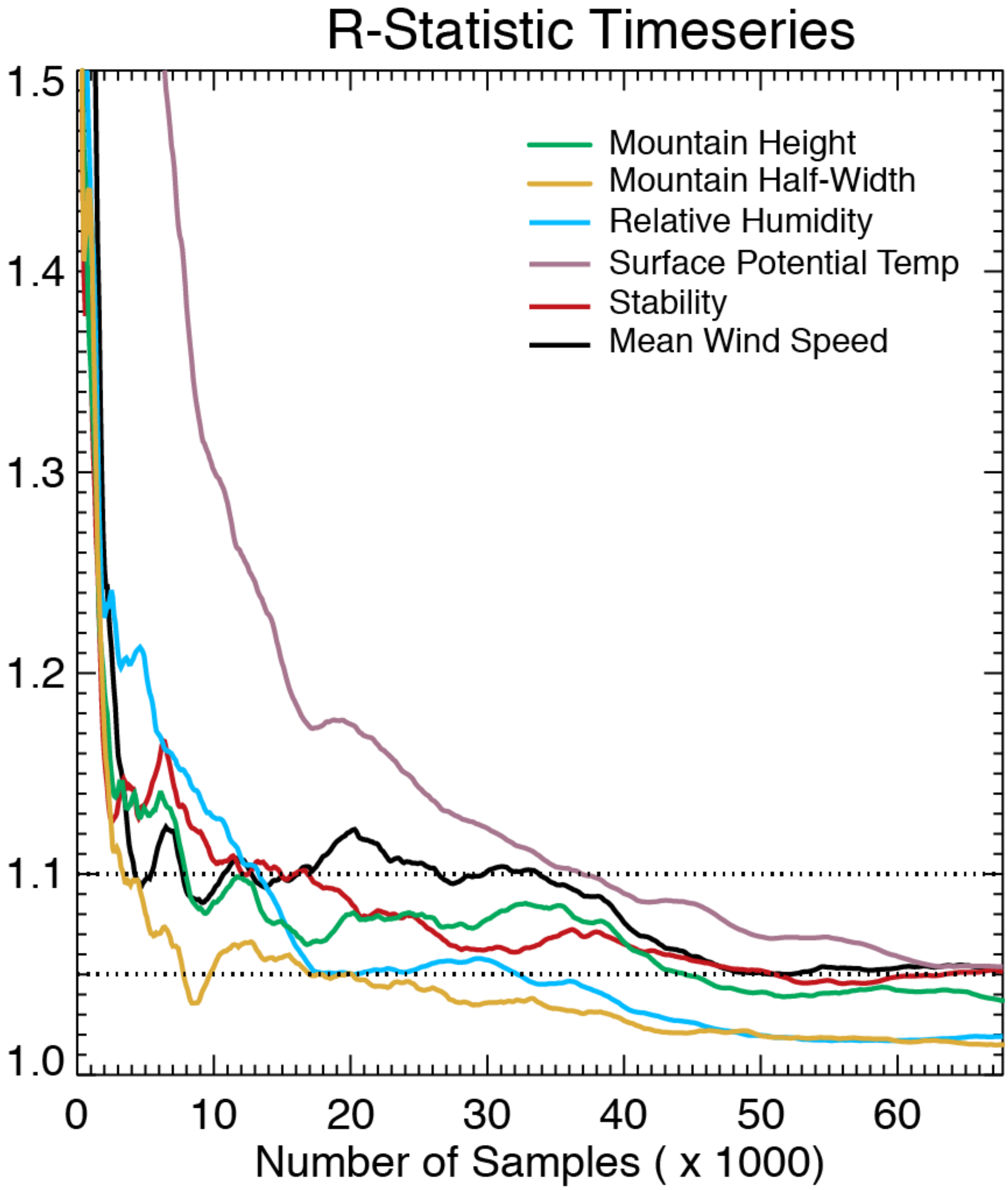

Figure 7. R-statistic ($\hat{R}$) values for each model input parameter, for successively greater numbers of samples.

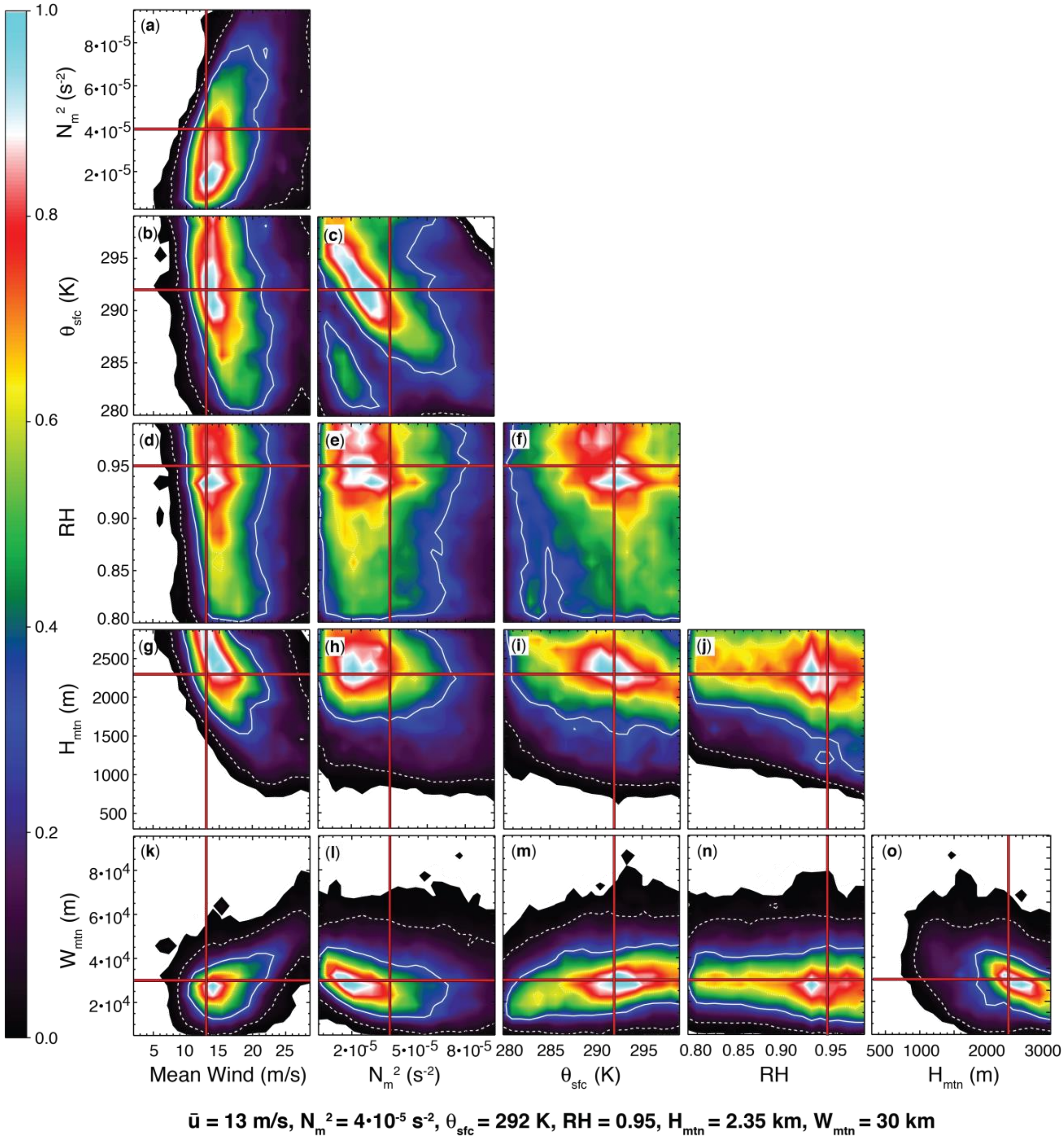

Figure 8. Posterior two-dimensional marginal PDFs for all pairs of input parameters from the MCMC experiment. As in Fig. 5, red lines indicate the parameter value used in the control case. White solid and dashed lines contour the 68% and 95% probability mass, respectively. Bright colors at any point imply a high probability that the parameter combination at that point produced precipitation output similar to the control output.

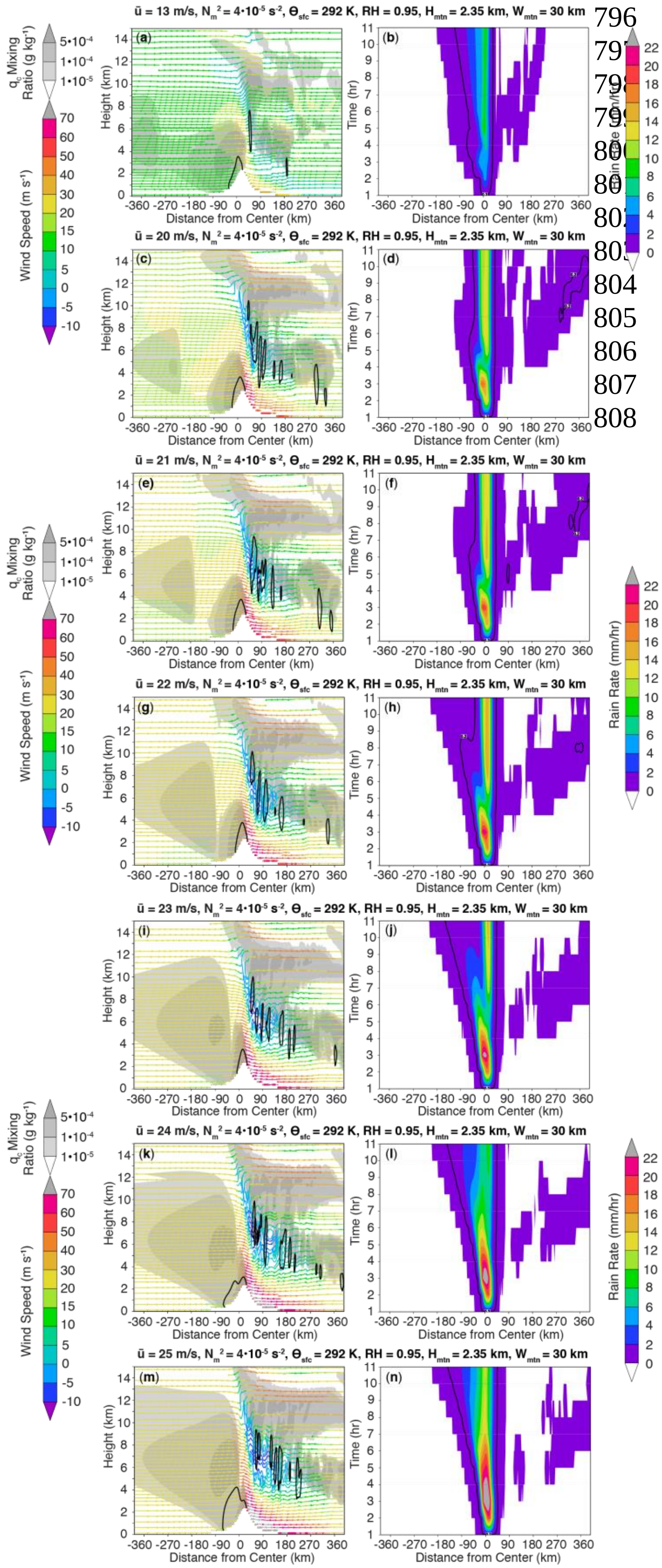

Figure 9. Contours, shading, and colors as in Fig. 3. X-Z cross-sections of the model domain during last hour of simulation (*first column*). Hovmöller diagrams of precipitation rate (*second column*). Each row represents model output for varying wind speeds: 13 m s^{-1} (control case; *a*,*b*), 20 m s^{-1} (*c*,*d*), 21 m s^{-1} (*e*,*f*), 22 m s^{-1} (*g*,*h*), 23 m s^{-1} (*i*,*j*), 24 m s^{-1} (*k*,*l*), and 25 m s^{-1} (*m*,*n*).

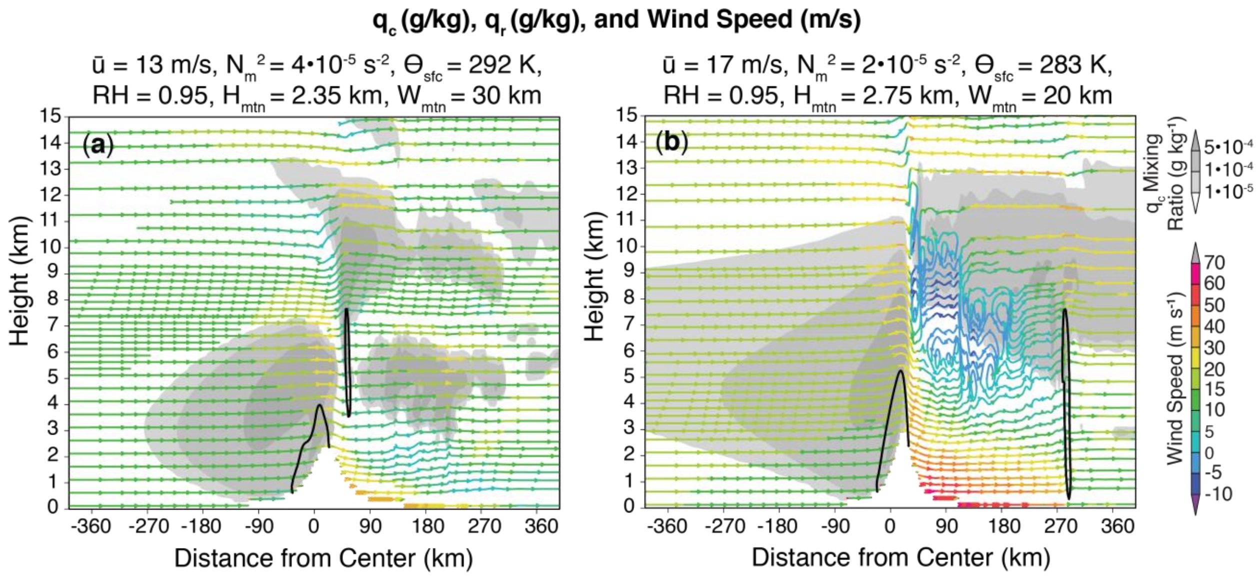

Figure 10. Contours, shading, and colors as in Fig. 3a. *(a)* X-Z cross-section of control case. *(b)* X-Z cross-section of the second MCMC high-probability mode, as described in Section 4.

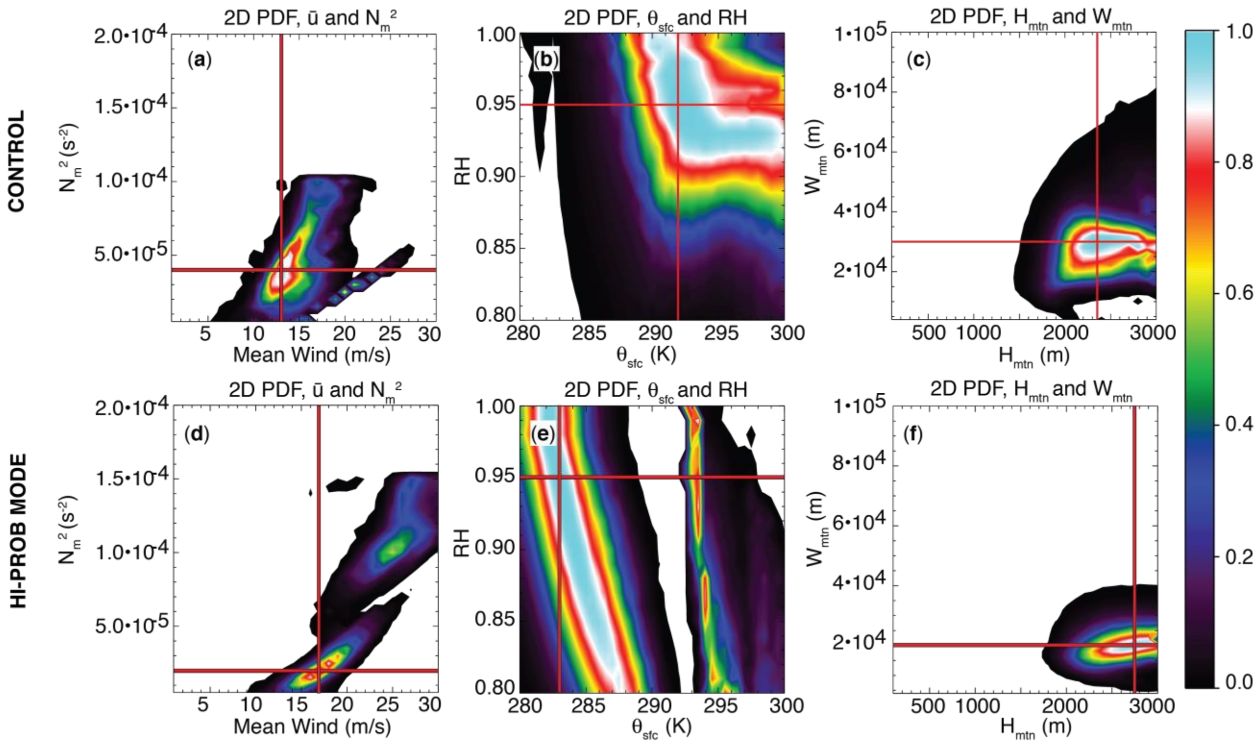

Figure 11. Contours, lines, and shading as in Fig. 5. The *first column* contains 2D joint PDFs of wind speed and stability; the *second column* contains 2D PDFs of surface potential temperature and relative humidity; and the *third column* contains 2D PDFs of mountain height and half-width. The *first row* represents the control case; the *second row* represents the second MCMC high-probability mode.

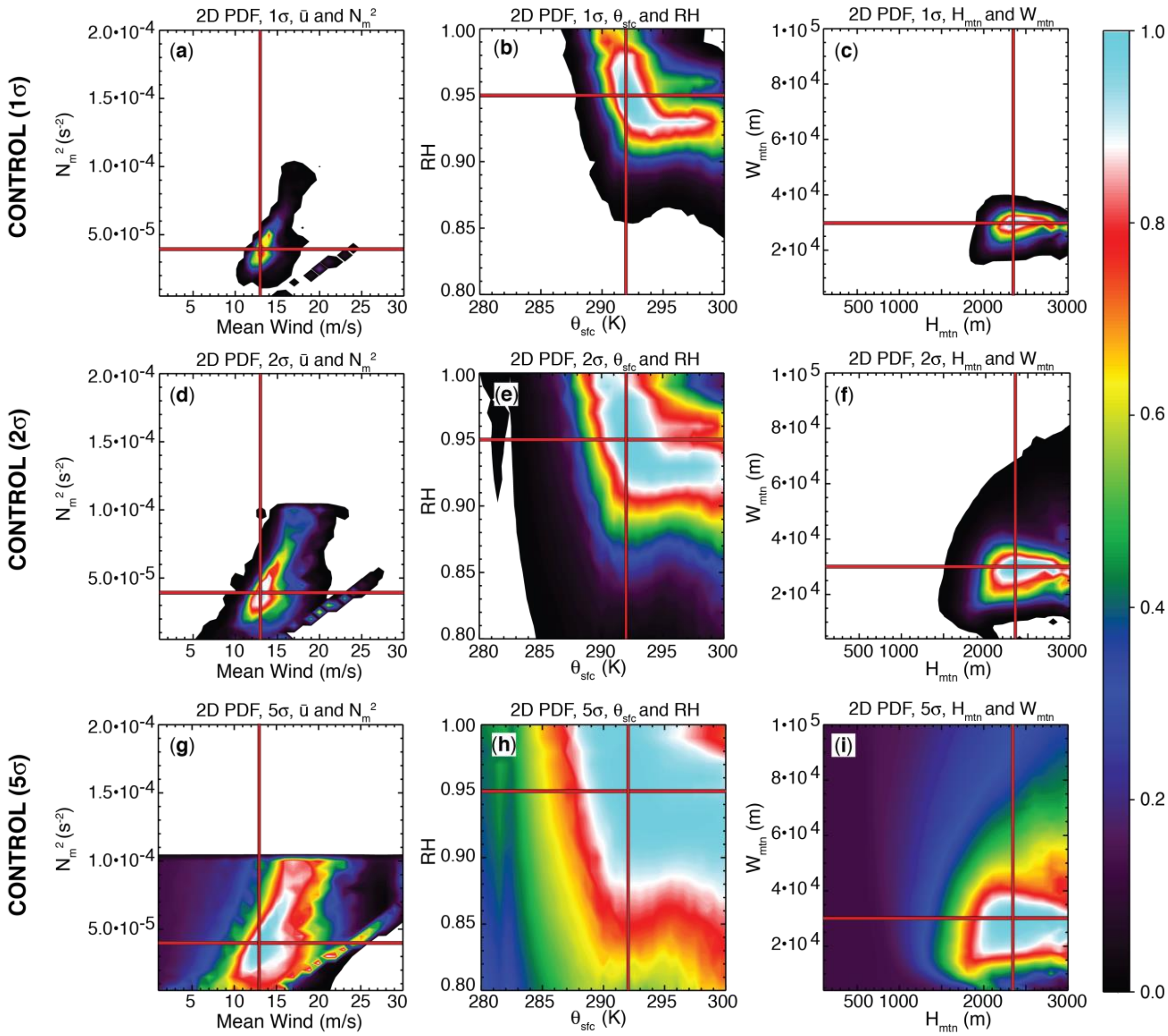

Figure 12. Contours, lines, and shading as in Fig. 5. The *first column* contains 2D joint PDFs of wind speed and stability; the *second column* contains 2D PDFs of surface potential temperature and relative humidity; and the *third column* contains 2D PDFs of mountain height and half-width. The *first row* represents the control case with $1s$ error; the *second row* represents the control case with $2s$ error; and the *third row* represents the control case with $5s$ error.